Supplementary Materials for

Alternating sequences of future and past behavior encoded within hippocampal theta oscillations

Mengni Wang, David J. Foster, Brad E. Pfeiffer*

*Corresponding author. Email: brad.pfeiffer@utsouthwestern.edu

Published 9 October 2020, *Science* **370**, 247 (2020)
DOI: 10.1126/science.abb4151

This PDF file includes:

Other Supplementary Materials for this manuscript includes the following:
(available at science.sciencemag.org/content/370/6513/247/suppl/DC1)

MDAR Reproducibility Checklist (.pdf)

Materials and Methods

Behavior and data acquisition

The datasets used in this study were previously reported, as were the details of the behavior and data acquisition methods(*11*, *12*). Briefly, after handling, adult male Long-Evans rats were trained to explore a 1.8-meter-long linear track for chocolate milk reward at either end of the track. The rats were then trained to explore a 2-meter x 2-meter square arena with 36 evenly spaced wells embedded in the arena floor for chocolate milk reward. The linear track behavior was memory independent; the rat was rewarded on each end of the track after every traversal. The open field behavior was a working memory dependent task in which the rat alternated between random foraging and goal-directed navigation to a recently learned, hidden location(*11*). Following training, rats were implanted with custom-built microdrive arrays (25-30g) housing 40 independently adjustable, gold-plated tetrodes (twisted bundles of four 17.8 μm 90% platinum/10% iridium wires, California Fine Wire), aimed at bilateral area CA1 of dorsal hippocampus (20 tetrodes/hemisphere; 4 mm posterior, 2.85 mm lateral to bregma). Tetrodes were individually lowered to their final recording locations over 1-2 weeks following implantation. A bone screw firmly attached to the skull served as ground. All neural data were collected using a Neuralynx (Bozeman, MT) data acquisition system at 32,556 Hz synchronized with an overhead video system recording behavior at 60 Hz. Animal position on each video frame was identified as the central location between green and red LEDs (respectively positioned at the front and back of the microdrive array), roughly corresponding to the center of the rat's skull. Action potentials (threshold crossings > 50 μV above baseline) were recorded at 32,556 Hz and continuous local field potential (LFP) was digitally filtered between 0.1 and 500 Hz and recorded at 3,255.6 Hz. Individual units were identified by manual clustering based on spike waveform amplitudes using custom software (xclust2, Matt A. Wilson). Putative excitatory and inhibitory units were identified on the basis of spike width and mean firing rate(*11*). For each tetrode, one representative electrode was selected for LFP analysis. Only tetrodes on which excitatory hippocampal cells were recorded were used; thus all LFP signals were recorded in the CA1 pyramidal layer (as confirmed by post-experiment lesions and histology(*11, 12*)).

To allow direct comparison between theta sequences arising during exploration of linear track vs. open environments, we restricted our analysis to three rats that performed both open field and linear track behaviors on consecutive days, with minimal movement (< 100 μm travel) of tetrode wires between days to ensure that the recording sites were similar across environments. However, because we did not record continuously during the home cage rest/sleep periods between experiments, we were not confident in our ability to identify the same units across consecutive experimental days, and our analysis assumes that each recording session represents an independent neural population. For all recording sessions, the rat subject had explored the environment in its current position in the recording room for at least one prior session (during training or during a previous recording session); thus, the environment is not novel for any session.

Place fields, spatial information, and decoding

Position was binned (2 cm) and position tuning curves ('place fields') were calculated as the smoothed (Gaussian kernel, sigma = 4 cm) histogram of firing activity normalized by time spent per bin. Only periods of movement (velocity ≥ 5 cm/s) were used to determine firing activity and occupancy. Units were considered to have a place field if the unit was classified as excitatory(*11*) and the peak of the tuning curve was > 1 Hz; units not meeting these criteria were

excluded from further analysis. Place fields were defined as contiguous bins (minimum of 20 bins) with a firing rate greater than 20% of the maximum firing rate. Spatial information per spike for each unit was defined as the sum across all spatial bins of $p_i(\lambda_i/\Lambda)\cdot\log2(\lambda_i/\Lambda)$, where p_i is the occupancy probability of bin i, λ_i is the firing rate for bin i, and Λ is the mean firing rate of the unit(*6*). A memoryless, probability-based decoding algorithm was used to estimate spatial information expressed in the hippocampus at any given time window based upon unit place fields as previously described(*11*, *35*). Mean decoding error (Table S1) was quantified using non-overlapping 250 ms time windows during movement (velocity > 5 cm/s).

LFP analysis

To examine theta, the local field potential (LFP) was band-pass filtered between 6-12 Hz, and theta power was defined as the absolute value of the smoothed (Gaussian kernel, sigma = 300 ms) Hilbert transform of this filtered signal. 0°/360° was defined as the trough of the filtered oscillation. One centrally located tetrode within stratum pyramidale was selected and the theta signal (phase, power, etc.) from this tetrode was used for analysis. Individual theta oscillations were excluded from analysis if they occurred during periods of immobility or slow movement (velocity < 10 cm/s), if they had a trough-to-trough duration of less than 80 ms (> 12.5 Hz) or more than 160 ms (< 6.25 Hz), or if the phase was not monotonically increasing throughout the entire oscillation. These criteria excluded 5.4% of running-related (velocity ≥ 10 cm/s) theta oscillations. The remaining theta oscillations were considered qualifying oscillations and were included in subsequent analysis. To examine beta, the raw LFP was band-pass filtered between 15-20 Hz, and beta power was defined as the absolute value of the smoothed (Gaussian kernel, sigma = 150 ms) Hilbert transform of this filtered signal.

Theta sequence quantification

Unless otherwise specified, spatial information was decoded using 20 ms windows advanced in 5 ms increments for times when the rat's velocity was equal to or above 10 cm/s. Windows with zero spikes were excluded from further analysis. For some analyses (Figs. S7 and S8), 10 ms non-overlapping windows were used, as described in the figure legend. Each decoded frame was assigned the theta phase nearest the central time point of the decoding window. Each decoded frame was shifted in the *x* and *y* dimensions for open field sessions or along the long axis of the track for linear track sessions, so that the rat's current physical location at the time of each decoded frame was centered, and then was rotated so the rat's current movement direction was upward. The rotated frame was then summed across the resulting *x* dimension to produce a linear posterior probability map behind/ahead of the animal. For each theta oscillation, a two-dimensional matrix was produced by aligning the above decoded frames in temporal order, resulting in a matrix similar to Figure 1A (the *x*-axis represents theta phase and the *y*-axis represents relative location). Probability histograms (*e.g.*, Figure 1B) were generated by identifying the phase of maximal posterior probability for each position bin across all qualifying theta sequences and normalizing the resulting histogram at each phase bin. Statistical quantification of the average forward and reverse components was determined based on 500 shuffles of each theta oscillation of either theta phase (the phase for each decoding window was randomly shuffled) or cell ID (the place fields for each cell were randomly shuffled and the entire session was decoded and analyzed as above).

To quantify the significance of individual theta sequences, a Sequence Score(*36*) was calculated for a matrix of posterior probabilities across position and time. A weighted best-fit line was calculated for the matrix. For each time bin, posterior probabilities within 10 cm of this line were summed and the average across all time bins was calculated. If the best-fit line

location was outside of the environment, the median decoded value was used instead. Sequence Scores range from 0 to 1; a Sequence Score of 1 indicates that all posterior probabilities reside within 10 cm of the best-fit line and represents a strong spatial sequence. The slope of the best-fit line determined the directionality of the spatial trajectory, with positive slopes signifying that the encoded path moved forward in the direction of the rat's heading direction. Sequence Score significance for individual theta oscillations or individual forward window or reverse window sequences was calculated as a Monte-Carlo *p*-value using 500 shuffles of cell ID or posterior probability (rotating the posterior probability for each decoding window). Sequences with a Sequence Score *p*-value ≤ 0.05 were considered significant.

Unimodal/bimodal cell classification

Only running periods (velocity $\geq$ 10 cm/s) were analyzed. For each putative excitatory unit, every spike was assigned the nearest theta phase. For units with a significantly non-uniform distribution of theta phases (circular Rayleigh test, $p \leq 0.05$), a smoothed (Gaussian, sigma 12°) histogram (10° bins) of firing activity was quantified. This smoothed histogram was converted into a firing rate index (FRI) by normalizing by the maximum value and then subtracting the resulting minimum value (giving values from 0 up to a possible maximum of 1). All local maxima in the FRI were identified, and those greater than 1/10th the overall maximum of the FRI with a prominence ≥ 0.05, a half-height width $\geq 30°$, and at least 50° from the nearest local maxima were considered to be peaks of activity. Units with a single peak of activity were classified as unimodal cells (569 units across all linear track sessions; 472 units across all open field sessions) and units with two peaks were classified as bimodal cells (275 linear track units; 282 open field units). Units with fewer than 100 spikes during movement, statistically uniform theta phase distribution, or more than two peaks were unclassified and excluded from further single-cell analyses, although these units were still included in probability decoding analyses. Proportion of spatial representation for unimodal vs. bimodal cells in the forward or reverse window was quantified by performing decoding for every time window with only unimodal or only bimodal neurons and normalizing the resulting probability across both, as for decoding with direction-specific place fields on a linear track(*36*). L-Ratios calculated as previously described(*11*).

Phase precession/procession

For each unit, the place field was normalized by finding the peak firing rate (defined as normalized position 0) and the place field boundaries as described above (normalized position 1 and/or -1). For linear track sessions, UP and DOWN directions were analyzed separately; -1 was defined as the place field boundary that the rat entered, and 1 was defined as the place field boundary that the rat exited. For open field sessions, the place field boundary location with the largest Euclidean distance from the peak was defined as 1 (*i.e.*, all place fields were treated as if they were circular). If the rat was moving toward the place field peak (the angle separating the rat's movement direction from the direction to the place field peak was less than 90°), the normalized position was negative. If the rat was moving away from the place field peak, the normalized position was positive. Only cells which fired at least 100 spikes within the place field during running periods (velocity $\geq$ 10 cm/s) were included in phase precession/procession analyses. Phase-location heatmaps binned the normalized position (bin size = 0.1) and theta phase (bin size = 10°) and calculated a smoothed (2-D Gaussian, sigma 2 bins), normalized firing rate map for each cell. Statistical quantification of average phase-location relationships based on weighted correlations of mean phase-location heatmaps across unimodal and bimodal population compared to 1,000 shuffles per cell of either theta phase (the phase associated with each spike

was circularly shifted +/- 180°) or normalized position (the normalized position values for each spike were randomized). Significance of phase precession or phase procession for individual neurons was based on linear Pearson's correlations of raw spike phases and normalized positions within the major peak window or minor peak window.

Correlation between population activity and theta/beta power

For each session, mean theta or beta power was quantified for each qualifying theta oscillation and the oscillations were sorted into ten evenly sized groups based on power of the respective frequency band. For each group, the FRI was quantified (as described above) for each cell using only spikes obtained during that group's oscillations. The average FRI was quantified across all cells within the major peak and minor peak windows for each group. Quantification of statistical significance based on repeated measures correlation(*37*).

Phase shifting between Run and REM

Sleep periods were defined as periods of extended (> 60 s) immobility. Within identified sleep epochs, REM was isolated from slow-wave sleep (SWS) based on increased ratio of theta to delta (1-4 Hz) power lasting > 30 s. REM sleep periods meeting our criteria were not present in the following sessions: Rat 2, Linear Track Session 1; Rat 2, Linear Track Session 2; Rat 2, Open Field Session 2; Rat 3, Linear Track Session 1; Rat 3, Open Field Session 1; Rat 3, Open Field Session 2. REM periods in the remaining sessions had durations (mean ± SEM) of 63.4 ± 5.0 s. Only cells with at least 70 spikes and a non-uniform distribution of spikes per theta phase (circular Rayleigh test, $p \leq 0.05$) during REM were analyzed. For each qualifying cell, the mean circular firing phase was quantified during Run (velocity ≥ 10 cm/s) periods in the behavior arena (open field or linear track) and during identified REM periods.

Ripple and replay analysis

Sharp-wave/ripples were detected as peaks (minimum 3 SD above the mean) in the smoothed (Gaussian, sigma 12.5 ms) ripple (150-250 Hz) power averaged across all tetrodes with single units, using only periods of immobility (velocity < 5 cm/s). The start and end of each ripple was defined as the point when the smoothed ripple power crossed the mean. Each ripple was decoded as described above, using 20 ms windows advanced in 5 ms increments. Linear track replay events were identified as ripples with an absolute value weighted correlation of the posterior probabilities (location vs. time) ≥ 0.6 and Monte-Carlo *p*-value ≤ 0.05 based on 1,000 cell ID shuffles. Directionality of replay events (forward vs. reverse) was quantified as previously described(*38*) based on decoding with place fields determined during only UP or DOWN runs on the linear track. To quantify the ratio of spikes in ripples to spikes in run (Figure 2C,D), the total number of spikes firing during running periods (velocity ≥ 10 cm/s) and the total number spikes fired during ripples was quantified for each cell, and a ratio of these values was calculated for each cell. Plotted is the mean and S.E.M. of those ratios. The data in Figure 2C is from all cells across all sessions; the data in Figure 2D is from linear track sessions (where the directionality of replay can be quantified).

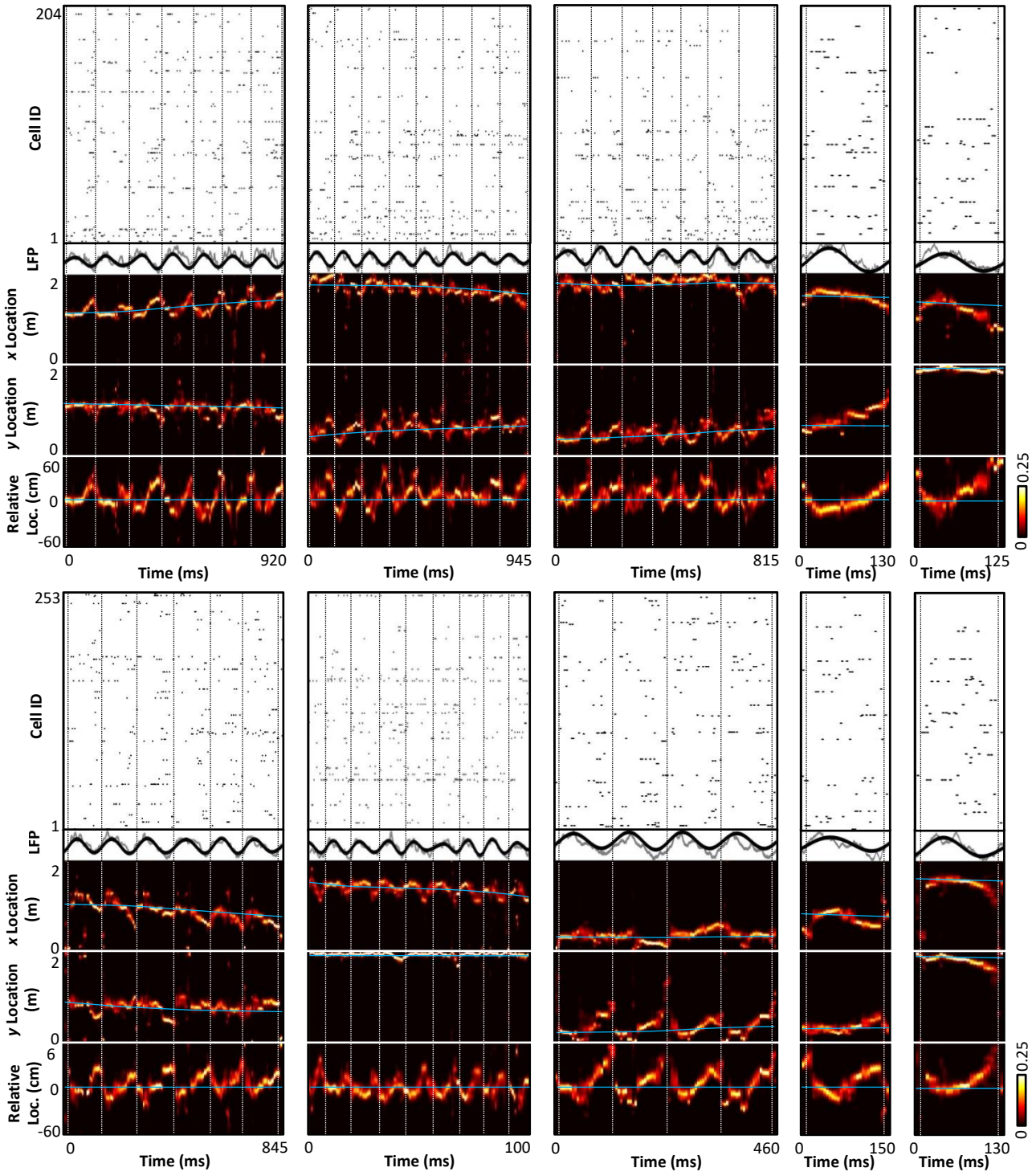

Fig. S1. Additional examples of forward and backward trajectories encoded in theta oscillations during open field exploration. Each example includes the raster plot (only putative excitatory neurons) of activity and LFP trace (raw = gray; theta-filtered = black). The posterior probability maps from the Bayesian decoding algorithm are summed across the *y* dimension to reveal the encoded position in only the *x* dimension. The same posterior probability maps are summed across the *x* dimension to reveal the encoded position in only the *y* dimension. Finally,

the posterior probability map for each decoding window was centered by the rat's physical location and rotated according to the rat's current running direction (so that 'up' is in the direction of the rat's movement); these maps were summed across the resulting *x* dimension to reveal the encoded position relative to the rat's current location (defined as 0) and movement direction (positive values indicate the direction of movement; negative values indicate locations 'behind' the rat). Cyan line indicates rat's actual location at each decoded frame. Vertical dashed lines indicate 70° theta phase. Some examples are replications of those in Figure 1 to show additional raster plot and *x* and *y* representation.

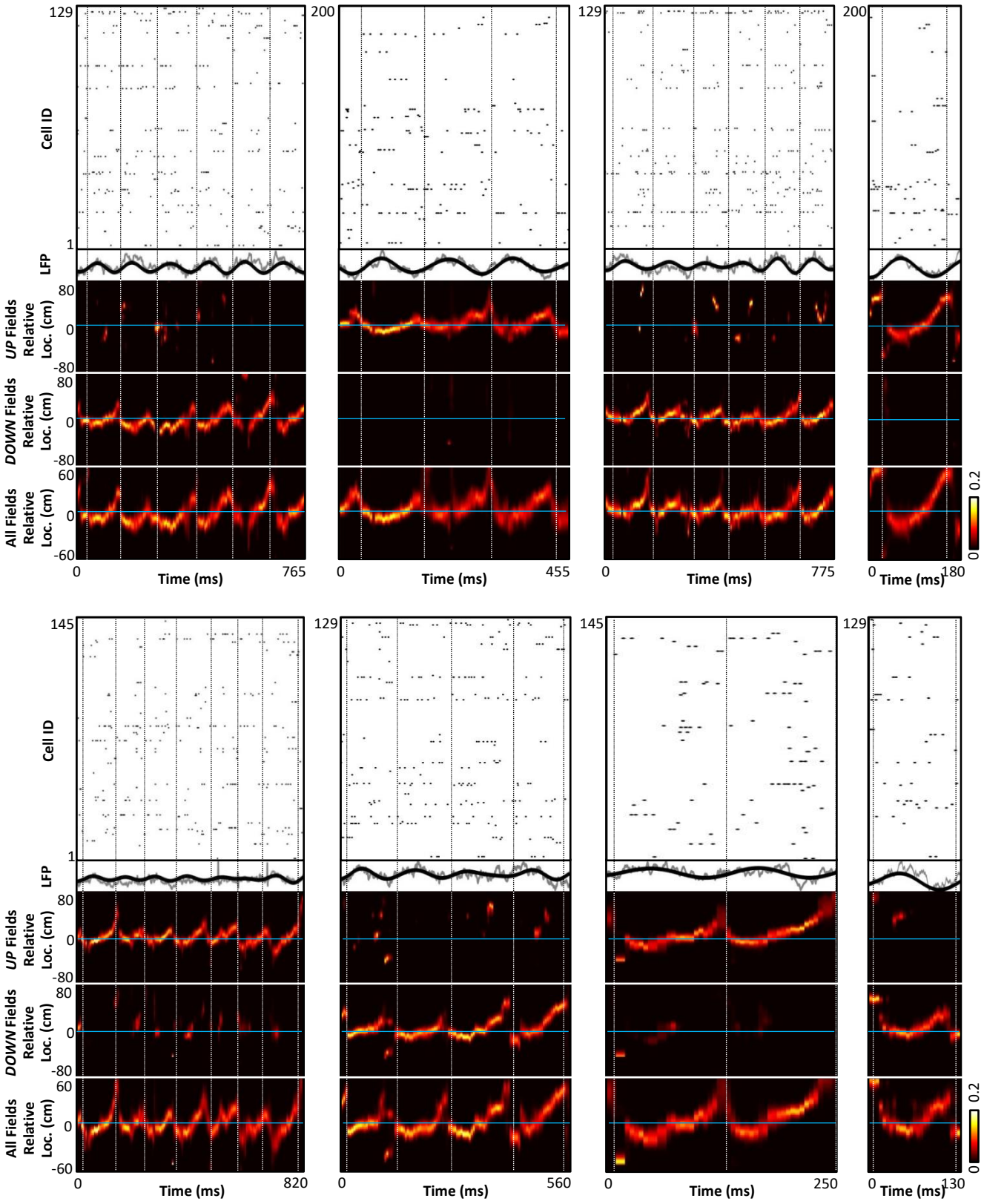

Fig. S2. Additional examples of forward and backward trajectories encoded in theta oscillations during linear track exploration. As Supplemental Figure S1, for linear track

exploration. Rather than sum across the *x* and *y* dimensions, each decoding window was centered by the rat's current physical location and rotated according to the rat's movement direction. The top decoding panel represents the decoding performed with place fields calculated exclusively during "UP" runs; the middle decoding panel represents the decoding performed with place fields calculated exclusively during "DOWN" runs; the bottom decoding panel represents the decoding performed with place fields calculated throughout the entirety of the behavioral session (in both directions of movement). Note that both the forward and reverse portion of the theta sequences were strongly encoded by place fields from a single direction.

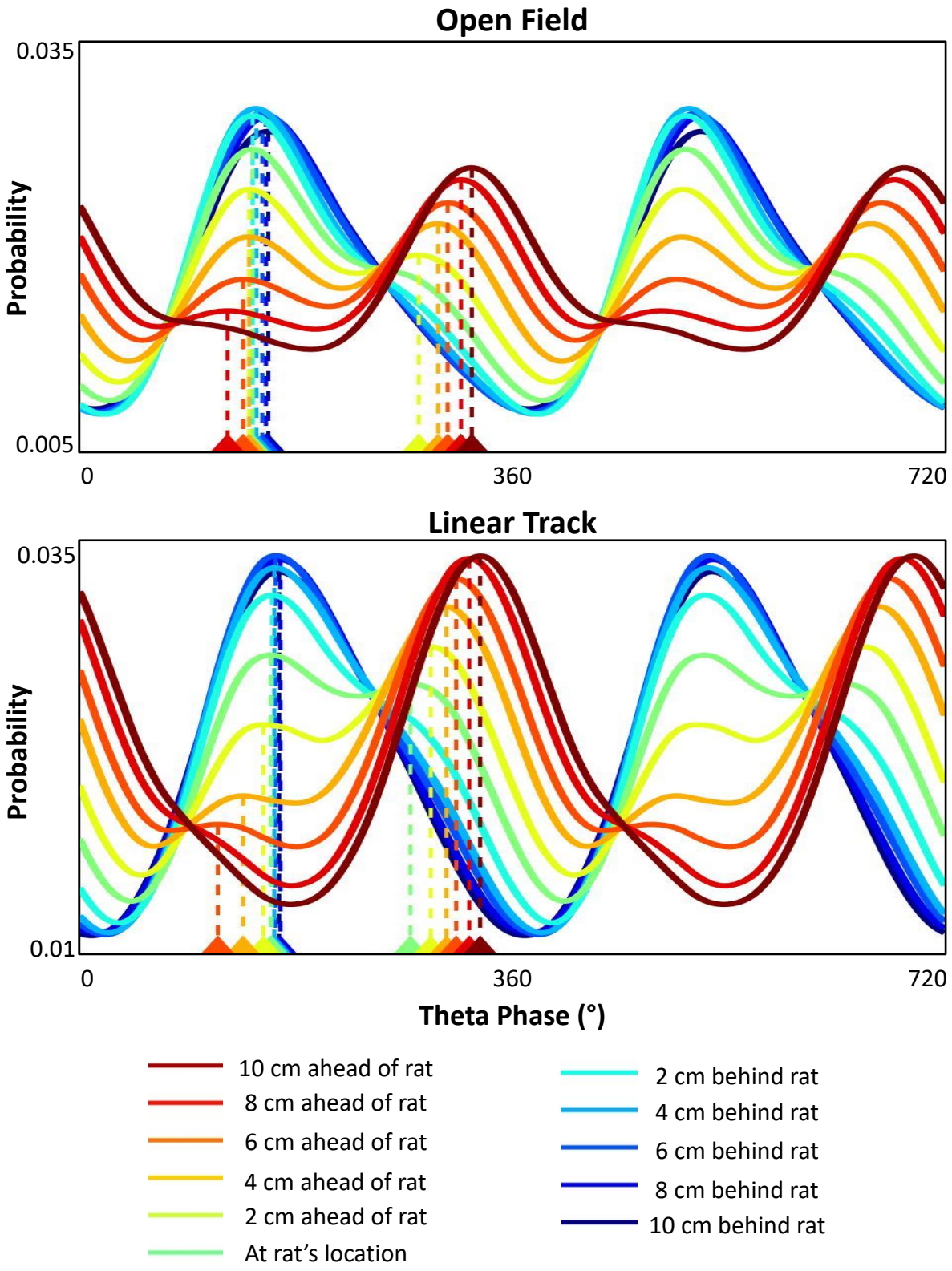

Fig. S3. Reverse and forward sequences in average theta oscillation. The data presented here are the same data from Figure 1B (top), plotted differently. For each position bin ahead or

behind the rat (different colors), the normalized histogram for that position bin from Figure 1B (top) was smoothed with a Gaussian filter (sigma 10°) (*i.e.*, the values from each row in the top graph of Figure 1b were smoothed and plotted here). Peaks in each plot are designated with a vertical dashed line, indicating the phase(s) at which that relative position is most likely to be represented. Note the clear sweep from ahead of the animal to behind the animal (the reverse of the animal's current movement direction) around theta phase 120° and the clear sweep from behind the animal to ahead of the animal (in the direction of the rat's movement) around theta phase 300°. For clarity, only position bins within 10 cm of the rat's current location are plotted here. (Position bins within 60 cm of the rat's current location are shown in Figure 1B.)

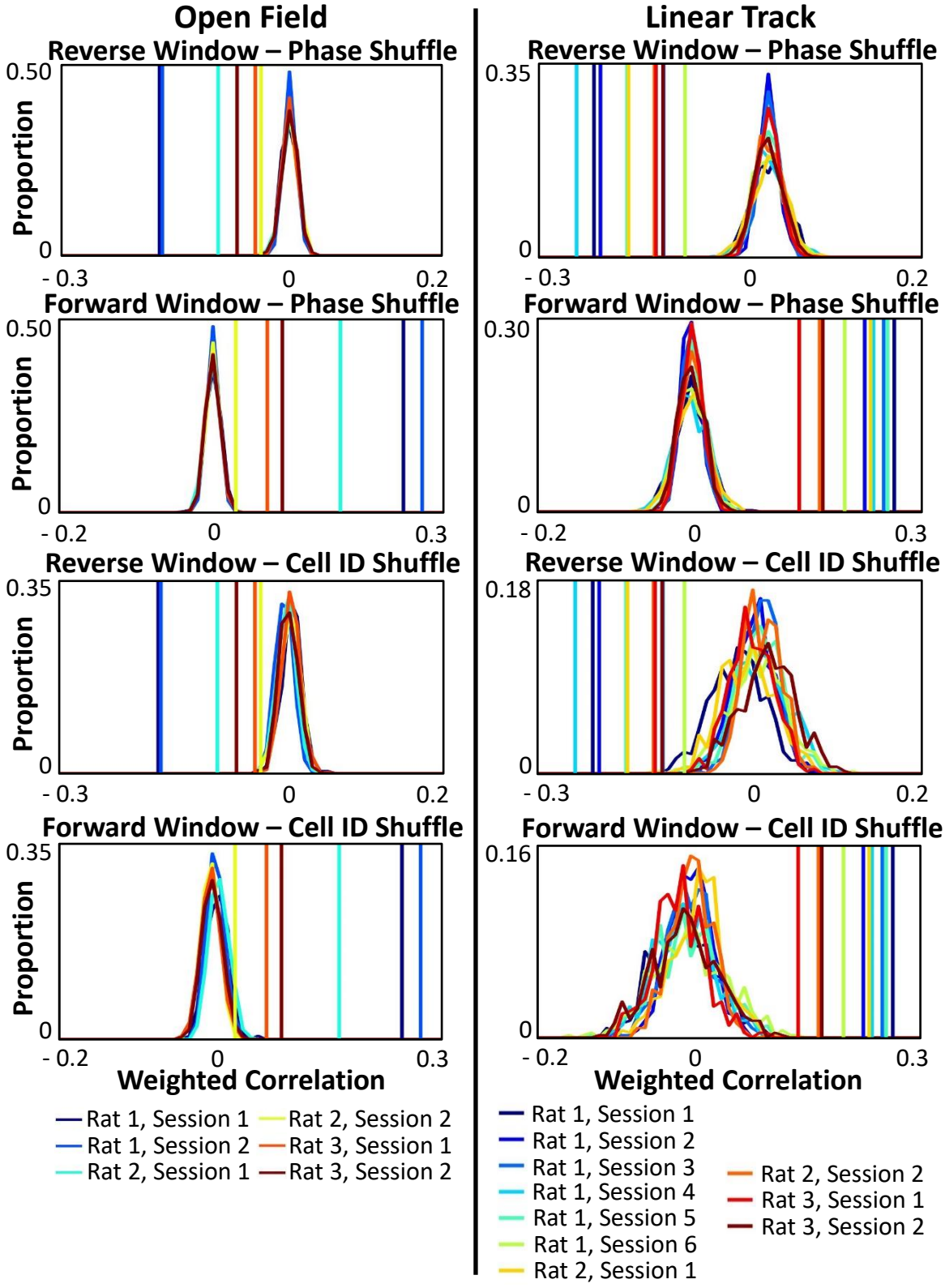

Fig. S4. Distribution of actual and shuffle values for each session. 500 cell ID shuffles and 500 theta phase shuffles were performed for each theta oscillation. The across-session summary

across all open field and linear track sessions is shown in Figure 1c. Plotted here are the same data separated by session. Curves denote the distribution of weighted correlation (theta phase vs. position) values for the shuffles. Vertical lines denote the mean weighted correlation for each session. All sessions have a Monte-Carlo p-value < 0.05 for both the forward and reverse window. All sessions have a positive weighted correlation (forward movement) in the forward window and all sessions have a negative weighted correlation (backward movement) in the reverse window.

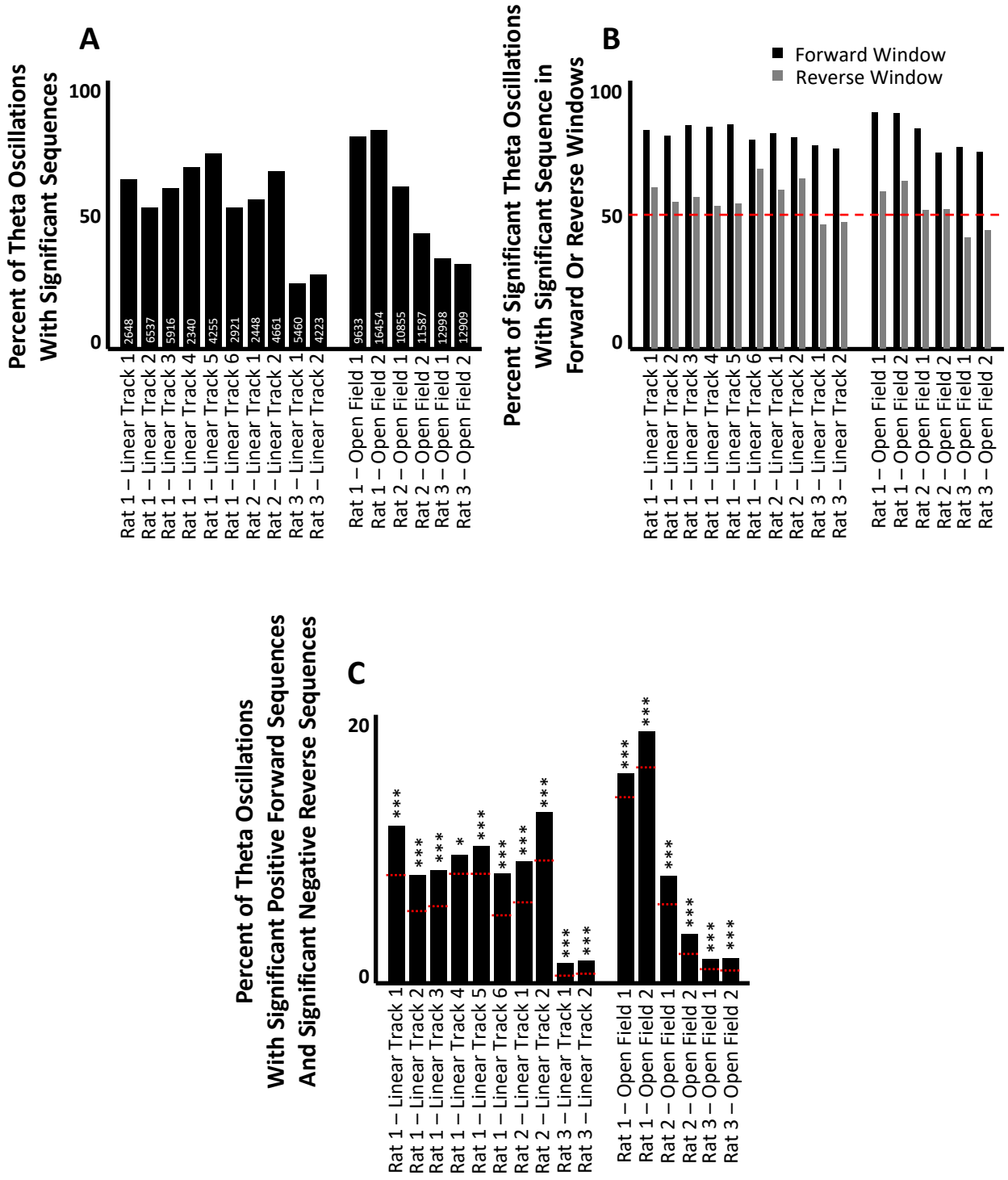

Fig. S5. Quantification of forward and reverse sequences for individual theta oscillations. For each theta oscillation, a Sequence Score was calculated in the forward and reverse windows (see Methods) that quantified how well those respective time windows encoded a virtual spatial trajectory. A Sequence Score was then calculated for 500 cell ID shuffles and 500 shuffles of the

posterior probability for each theta oscillation to determine statistical significance A Monte Carlo p-value ≤ 0.05 for both cell ID and probability shuffles indicated a significant spatial trajectory. **(A)** The percent of all theta oscillations per session with a significant Sequence Score in the forward and/or reverse window. Number of total theta oscillations in each session specified on each bar. The percent of significant theta sequences is strongly correlated to the number of simultaneously recorded neurons (Pearson's $r = 0.7993$; p-value $= 2.03 \times 10^{-4}$). **(B)** For theta oscillations with a significant Sequence Score anywhere in the theta oscillation (in either the forward or reverse window), the percent with a significant Sequence Score in the forward window (black) or reverse window (grey). Note that most oscillations have a significant Sequence Score in both the forward and reverse window. **(C)** The percent of all theta oscillations with both a significant positively sloped (moving ahead of the rat) Sequence Score in the forward window and a significant negatively sloped (moving behind the rat) Sequence Score in the reverse window. Red dashed lines represent chance levels based on the independent probabilities of a significant positively sloped sequence in the forward window or a significant negatively sloped sequence in the reverse window. For all sessions, the number of oscillations with both a forward sequence and a reverse sequence is well above chance. * p-value < 0.05; *** p-value $< 10^{-5}$; binomial cumulative distribution.

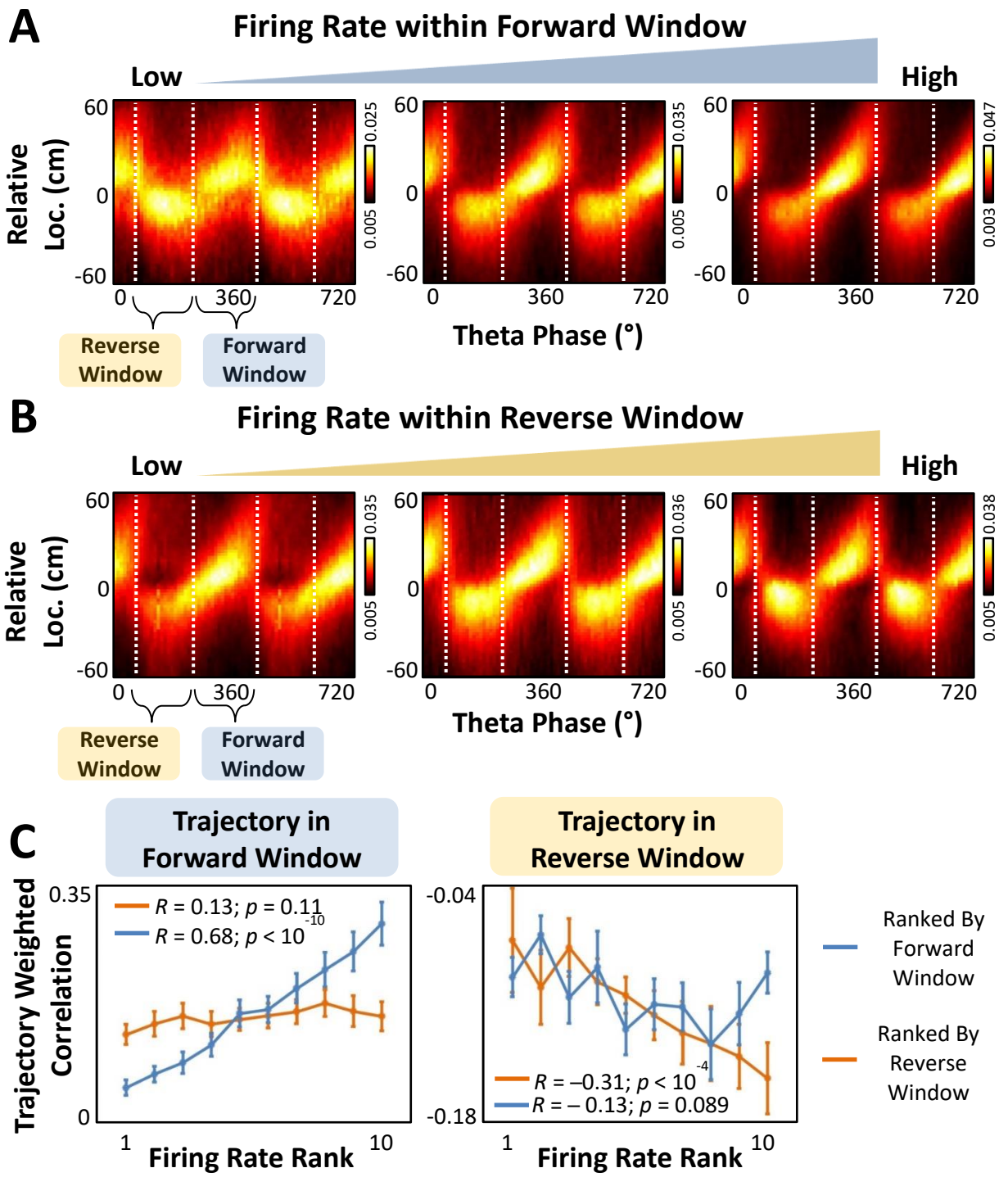

Fig. S6. Forward and reverse trajectories are independently regulated by firing in the forward and reverse windows. For each session, the population firing rate was quantified in the forward window and the reverse window for every theta oscillation (when the rat's velocity was above 10 cm/s) and ranked according to the firing in these windows. **(A)** Across-session average distribution of peak posterior probabilities for the third of theta oscillations in each session with the lowest population activity in the forward window (left), third of theta oscillations with the highest population activity in the forward window (right), and third of theta

oscillations in between (center). **(B)** As A, but ranked by population firing rate in the reverse window. As in A, the forward trajectory is present regardless of the amount of population activity in the reverse window, but the backward trajectory is strongly dependent upon the firing rate within that time frame. **(C)** Quantification of the weighted correlation in the forward window (left) or reverse window (right) as a function of population activity in the forward window (blue line) or reverse window (orange line), separated into ten ranks of population activity (n = 16 sessions). The forward trajectory (a positive weighted correlation) is statistically strengthened by increased population activity in the forward window, but not affected by firing rate changes in the reverse window. Likewise, the backward trajectory (a negative weighted correlation) is stronger (more negative) when there is increased activity in the reverse window, but is statistically unaffected by firing rates in the forward window. Statistics based on Pearson's correlation.

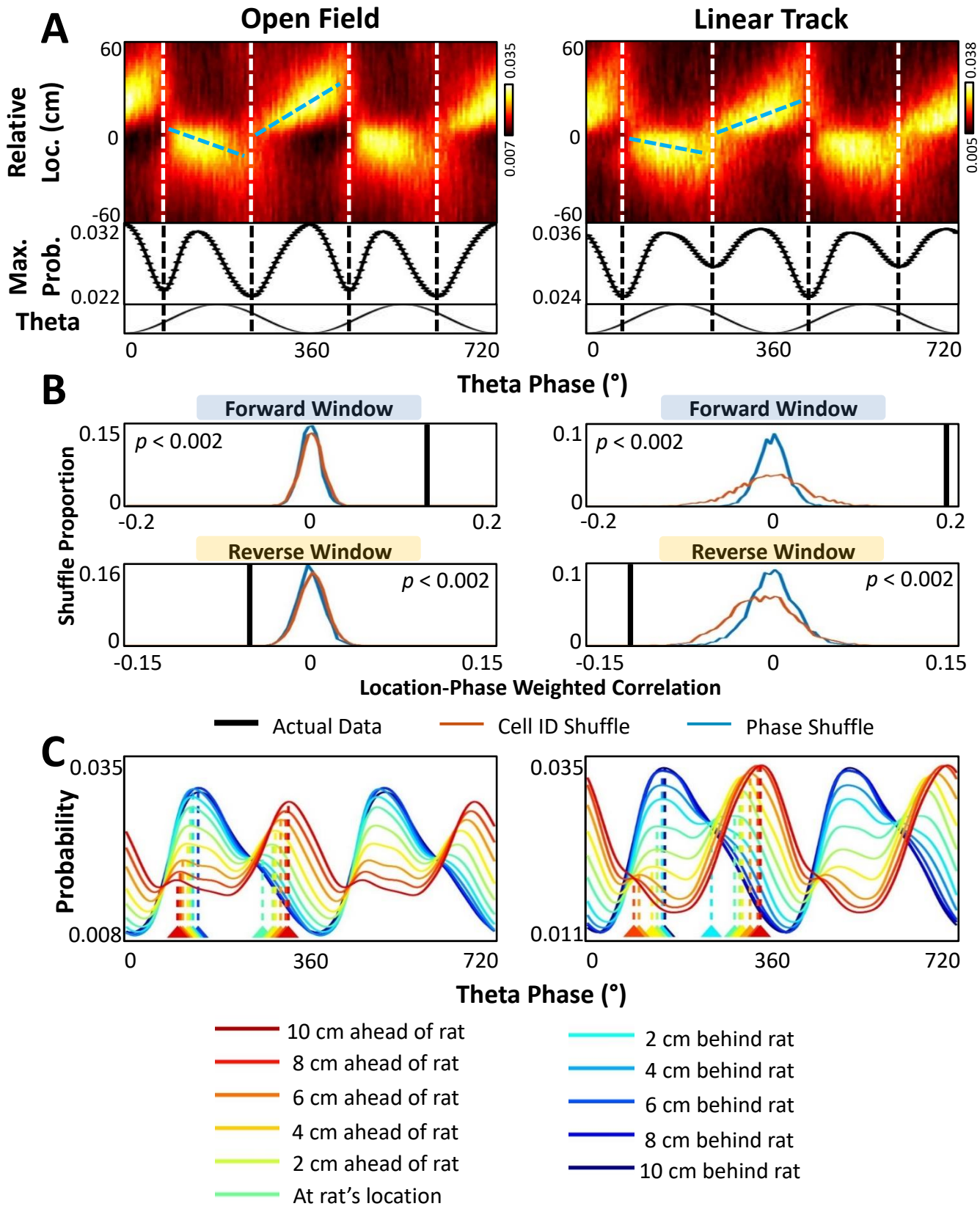

Fig. S7. Forward and reverse components of theta sequences are observed when the

decoding windows are non-overlapping. To test whether the reverse component of theta sequences was a trivial artifact of the temporal smoothing caused by using overlapping decoding windows, we repeated the analysis using 10 ms non-overlapping windows. **(A)** As Figure 1B, for 10 ms non-overlapping decoding. Top, probability histogram of theta phase (5° bins) with maximum posterior probability at each position relative to rat (2 cm bins) for the third of theta oscillations with highest firing near the peak of theta. Dashed cyan lines represent best fit lines (least squares). Middle, maximum value of each theta bin above. Vertical dashed lines indicate trough in maximum probability density. Bottom, idealized theta oscillation. **(B)** As Figure 1C, for 10 ms non-overlapping decoding. Actual and distribution of weighted correlation values for 500 theta phase or cell ID shuffles per theta oscillation in forward and reverse windows. **(C)** As Supplemental Figure S3, for 10 ms non-overlapping decoding. The data presented here are the same data from Supplemental Figure 7A (top), plotted differently. For each position bin ahead or behind the rat, the normalized histogram for that position bin from Supplemental Figure 7A (top) was smoothed with a seven-point Gaussian filter (*i.e.*, the values from each row in the top graph of Supplemental Figure 7A were smoothed and plotted here). Peaks in each plot are designated with a vertical dashed line, indicating the phase(s) at which that relative position is most likely to be represented.

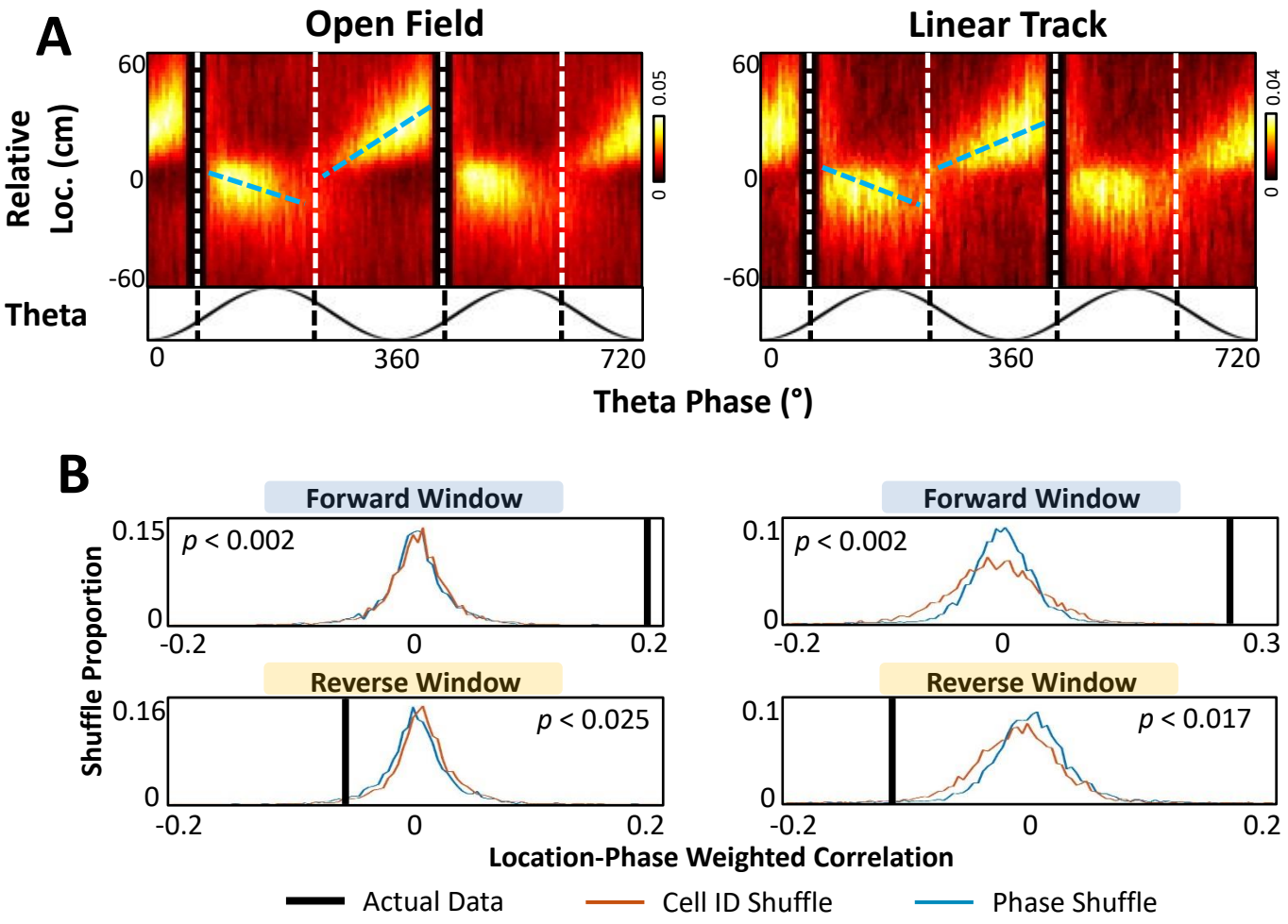

Fig. S8. Forward and reverse components of theta sequences are observed when decoding windows are restricted to single theta oscillations, when only theta oscillations with large numbers of cells are used, and when theta/delta ratio is high. (A) As Figure 1B, using non-overlapping 10 ms decoding windows and several additional criteria described below. These analyses test several alternate explanations for the observation of reverse theta sequences. All of these tests are performed together in the same analysis. First, they test whether the reverse sequence is a result of "bleed-through" from the previous forward sequence. The data presented in Figure 1 used 20 ms decoding windows and the data presented in Figure S7 used 10 ms decoding windows. Some of these windows spanned from the end of one theta cycle to the beginning of the next. To test whether the reverse component of theta sequences was a trivial artifact of 'bleed-through' from the previous forward component, we independently analyzed each theta oscillation, ensuring that no decoding window spanned 70° (each decoding window only had spikes with phases below 70° or only had spikes with phases above 70°). Second, they test whether the observation of reverse sequences is due to poor decoding arising from low numbers of participating cells. In these analyses, we also excluded any theta oscillation in which fewer than five cells fired an action potential in the forward window and fewer than five cells fired an action potential in the reverse window. Finally, they test whether reverse sequences

arise during unusual theta oscillations in which the theta power is uniquely low. In addition to the normal inclusion criteria (velocity ≥ 10 cm/s, theta oscillation duration between 80-160 ms, and monotonically increasing phase, as described in the Methods), we further excluded any theta oscillation in which the ratio of theta power/delta power was less than 1. When including these additional criteria, we still observe significant forward and reverse theta sequences in the forward and reverse windows, respectively, indicating that the reverse component of the theta sequence is not a trivial result of bleed-through from the previous forward sequence, poor decoding from low cell participation, or unusual theta oscillations. **(B)** As Figure 1C. Actual and distribution of weighted correlation values for 500 theta phase or cell ID shuffles per theta oscillation in forward and reverse windows.

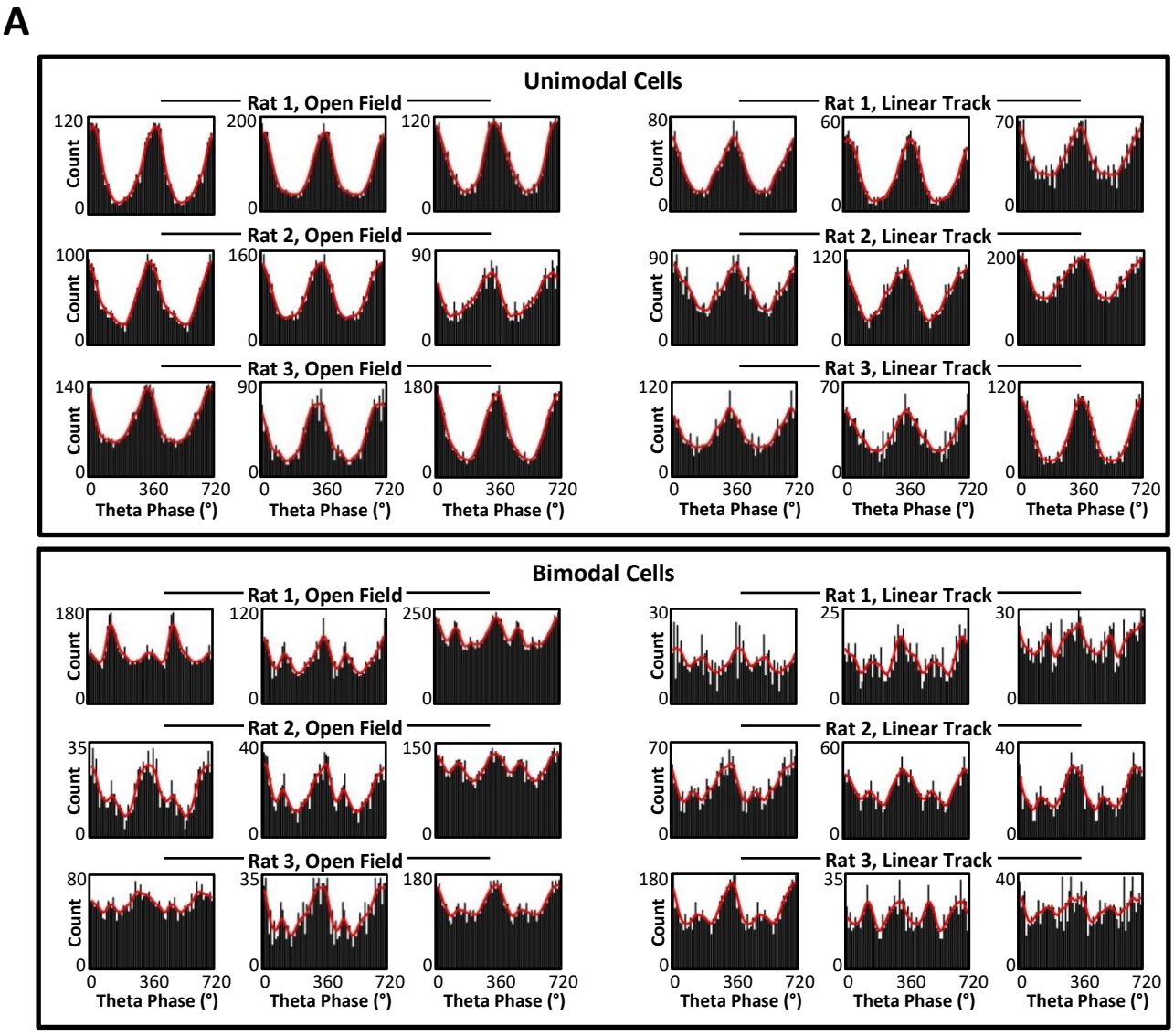

Fig. S9. Unimodal and bimodal cells. **(A)** Additional examples of unimodal (top) and bimodal

(bottom) cells from each rat recorded in open field (left) and linear track (right) sessions. Black, raw histogram of action potentials binned by theta phase (10° bins). Red, smoothed (Gaussian, sigma 12°). **(B)** Number of unimodal (red), bimodal (blue), and other (typically multimodal; white) cells for each session. Putative inhibitory neurons, neurons with insufficient numbers of spikes, and neurons with uniform distribution of spikes per theta phase (see Methods) are not included.

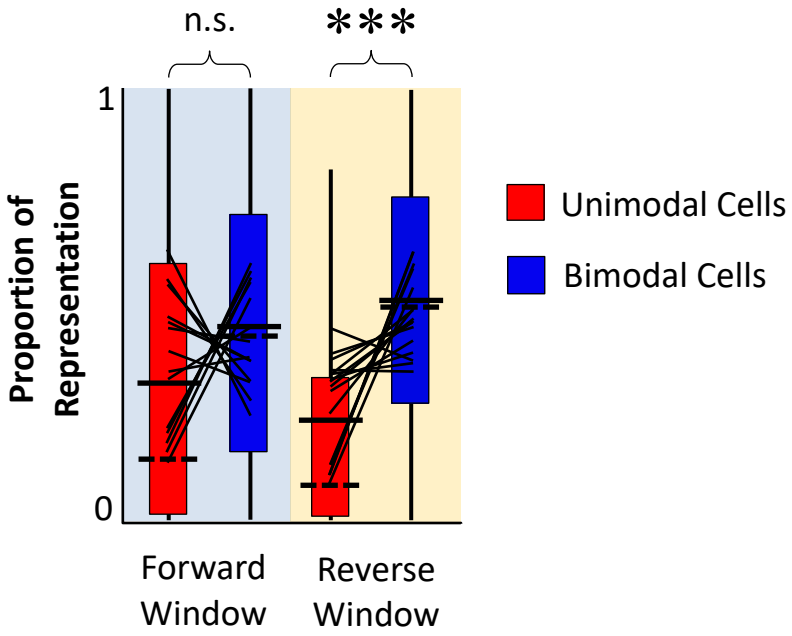

Fig. S10. Bimodal cells contribute more to reverse window representation than unimodal cells. Per-session box (quartile) and whisker (extreme range), mean (solid line), and median (dashed line) of decoding probability represented by unimodal (red) or bimodal (blue) cells in forward window (blue-shaded) or reverse window (yellow shaded). Lines indicate within-session means for each session. n.s. p-value > 0.05, *** p-value < 10^{-4}, Wilcoxon rank-sum test, n = 16 sessions.

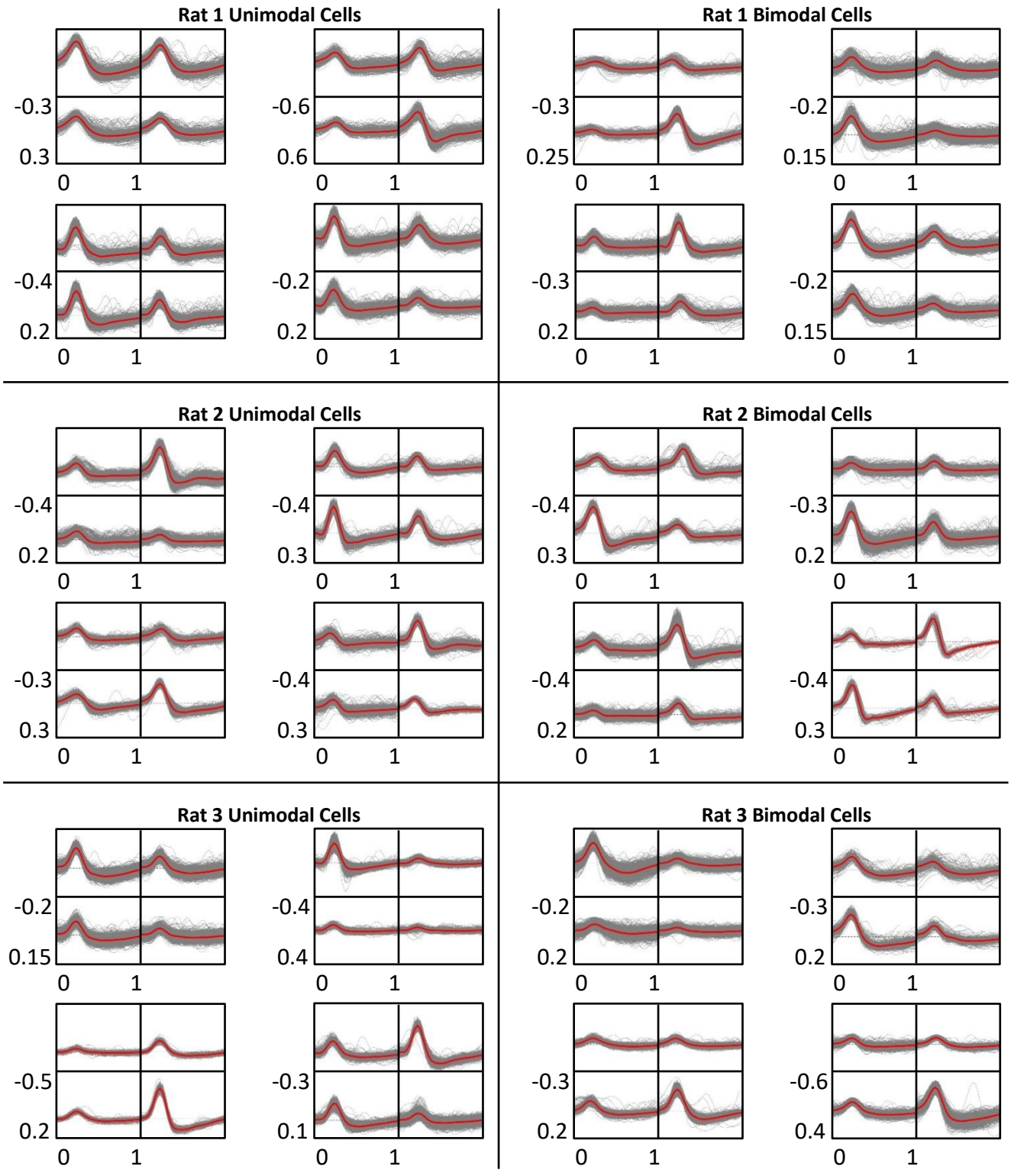

Fig. S11. Spike waveforms from example unimodal and bimodal cells. Spike waveforms from example unimodal (left) and bimodal (right) cells recorded from each rat. Gray traces

indicate each recorded spike; red trace indicates the average. For each cell, waveforms from all four electrodes of a tetrode are presented with identical scales; *y* axis is in mV, *x* axis is in ms. Note that *y* axis is inverted.

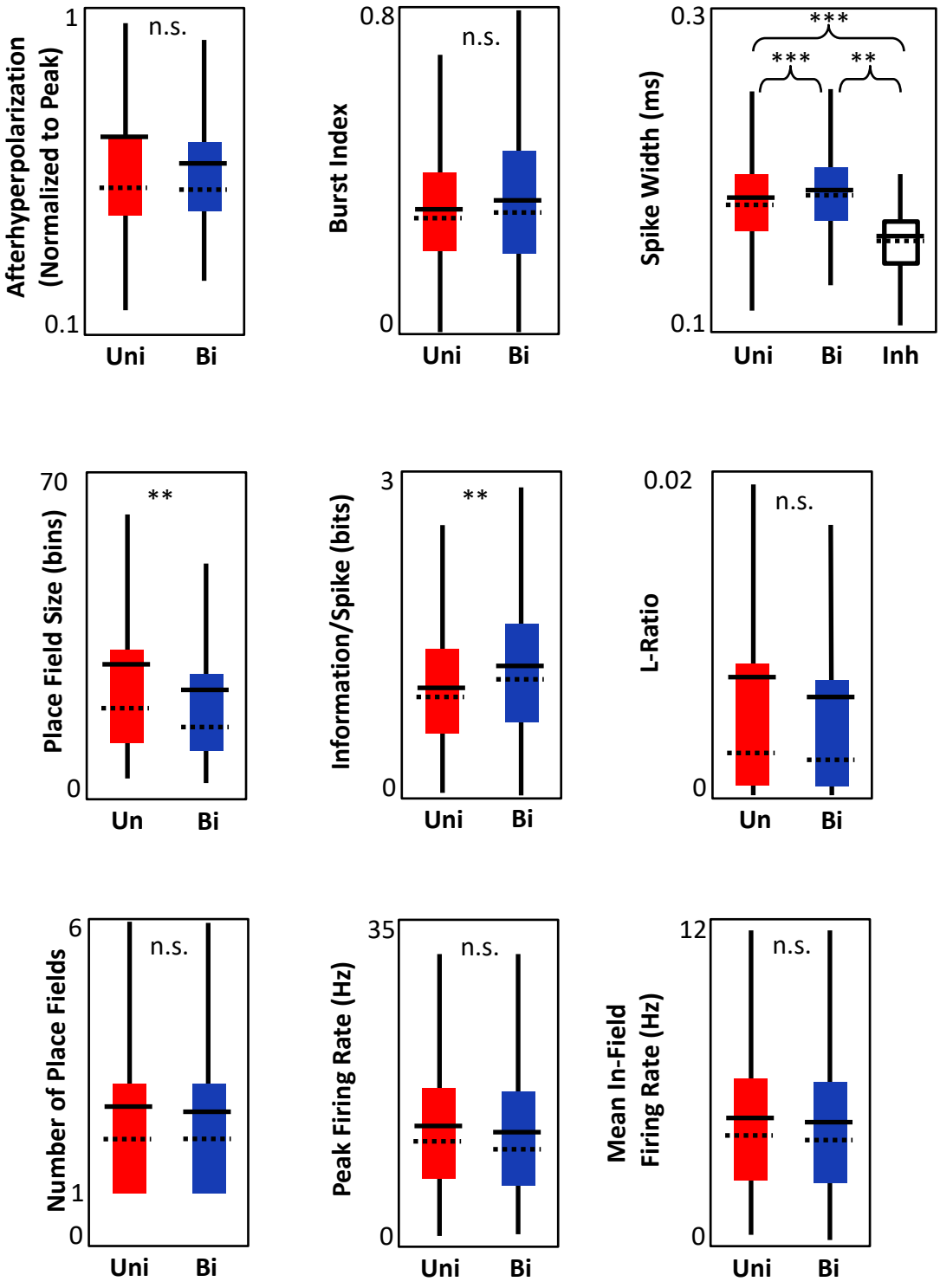

Fig. S12. Unimodal and bimodal cell properties. Box (quartile range) and whisker (extreme, non-outlier range) plot, mean (solid line), and median (dashed line) of after-hyperpolarization maxima (normalized by depolarization peak), burst index, spike width measured at half depolarization peak amplitude with inhibitory neuron population (Inh, n = 87), place field sizes,

information rate per spike, L-ratio (a measure of cluster quality), the number of place fields, peak firing rates, and mean in-field firing rates for all unimodal (Uni, n = 1,041) and bimodal (Bi, n = 557) cells. L-ratios are not significantly different, indicating that bimodal and unimodal cells have similar cluster quality and the observed bimodality in firing rates with respect to theta phase is not a trivial result of poor clustering. After-hyperpolarization and burst index are similar (burst index *p*-value = 0.06), but bimodal cells have a significantly slower action potential than unimodal cells. Note that both unimodal and bimodal cells have slower action potentials than fast-spiking inhibitory neurons recorded on the same tetrodes and are thus likely excitatory neurons. Number of place fields, peak firing rate, and mean in-field firing rate are not different between unimodal and bimodal cells. However, bimodal cells have significantly smaller place fields and a related increase in information per spike, suggesting they encode more spatially precise information. n.s. = *p*-value > 0.05, *** = *p*-value < 0.0001, Wilcoxon rank-sum test with Bonferroni correction for nine tests (original $\alpha = 0.05$; Bonferroni-corrected $\alpha = 0.0056$).

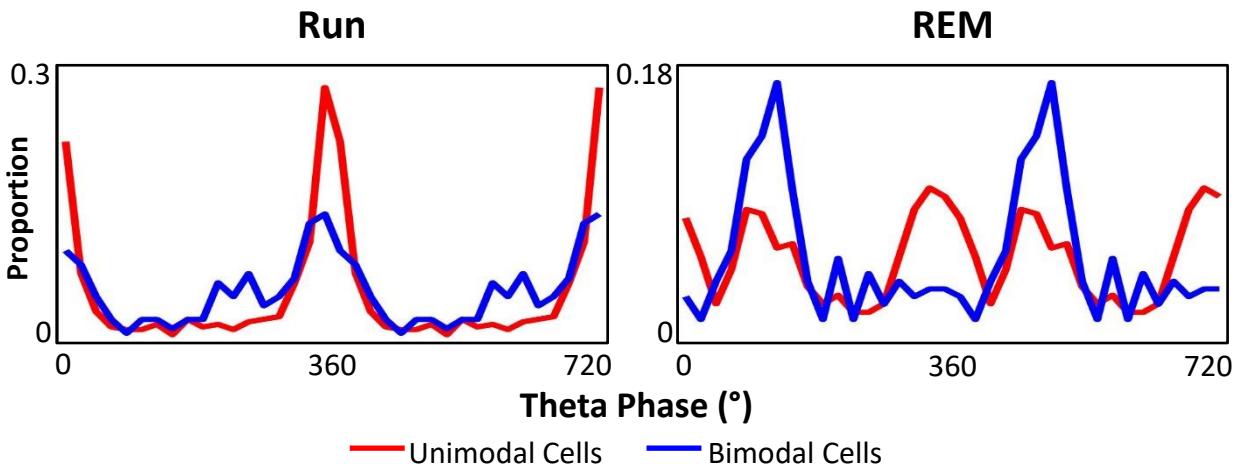

Fig. S13. Bimodal cells shift their preferred firing phase during REM sleep. For cells with sufficient numbers of spikes in Run and REM sleep, proportion of unimodal (red) and bimodal (blue) cells with circular mean firing rate per theta phase during exploration (Run) or during REM sleep immediately flanking behavior. Note that the circular mean firing phase for many bimodal cells during Run is between the major and minor peak (Fig 2).

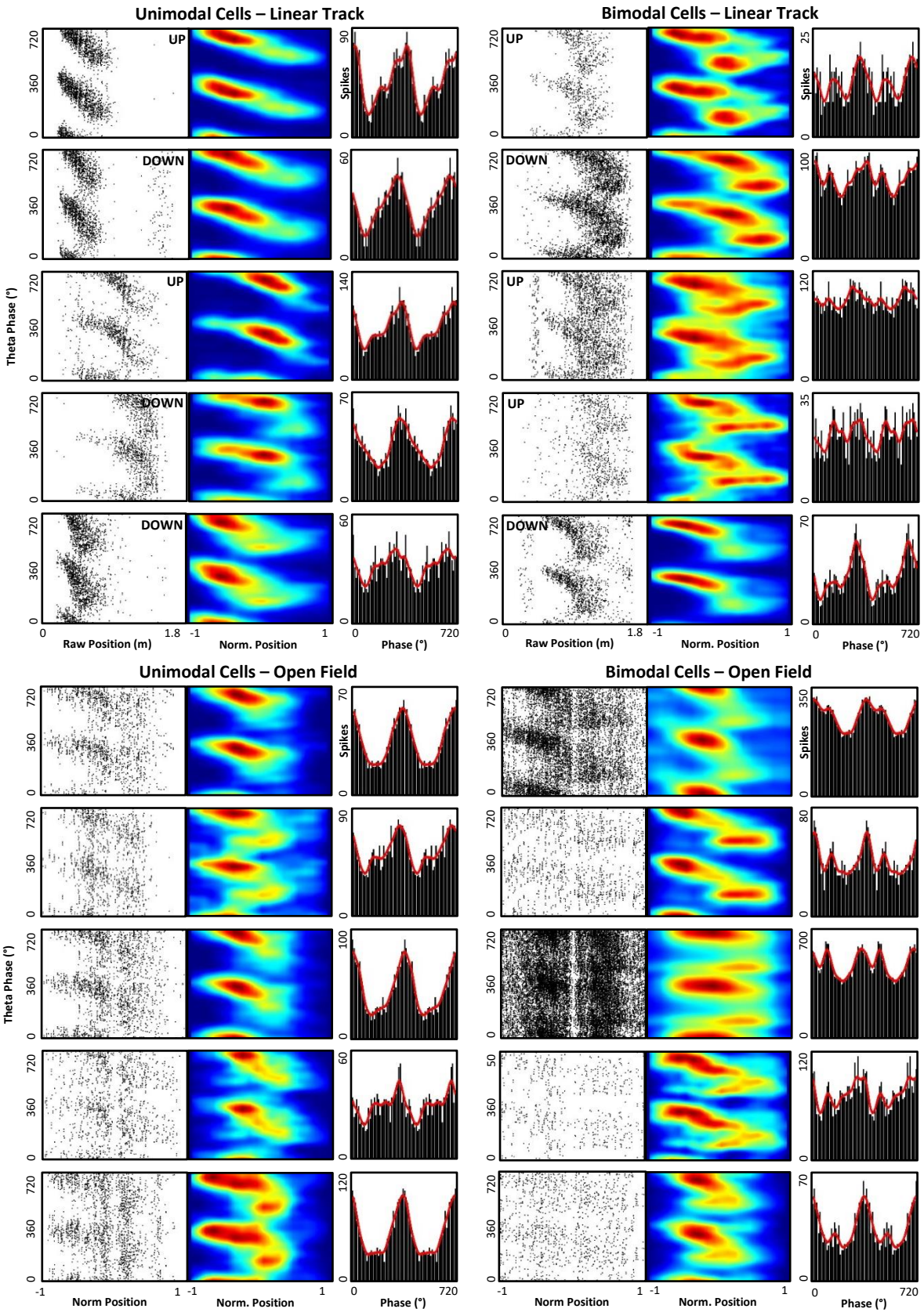
Unimodal Cells – Linear Track
Bimodal Cells – Linear Track
Unimodal Cells – Open Field
Bimodal Cells – Open Field
UP
DOWN
Theta Phase (°)
Spikes
Raw Position (m)
Norm. Position
Norm Position
Phase (°)

Fig. S14. Examples of phase precession and phase procession in unimodal and bimodal cells. Additional examples of unimodal (left) and bimodal (right) cells from linear track (top) and open field (bottom) sessions. For each linear track example, spikes and heatmap are shown for runs in the cell's preferred direction (IN or OUT). For each open field example, normalized position is relative to place field peak (normalized position = 0), place field boundaries (normalized position = -1 or 1), and rat's movement direction (toward place field center = negative position values; away from place field center = positive position values). For all examples and analysis, only spikes from periods of movement (velocity > 10 cm/s) are used. The heatmap is the smoothed (2-D Gaussian, sigma 2 bins), interpolated histogram of the spike plot on the left. The lack of spikes at normalized position 0 for open field sessions is because of lower numbers of passes through the place field's single central bin than through the outer bins (unlike for linear tracks, the rat is not forced to walk perfectly through each open field place field). The histogram of overall spikes per phase (used to categorize unimodal vs. bimodal) is plotted for each cell. Note that unimodal cells displaying phase procession during the minor peak window often have increased firing rates during that period that were not strong enough to meet our criteria for classification as bimodal cells.

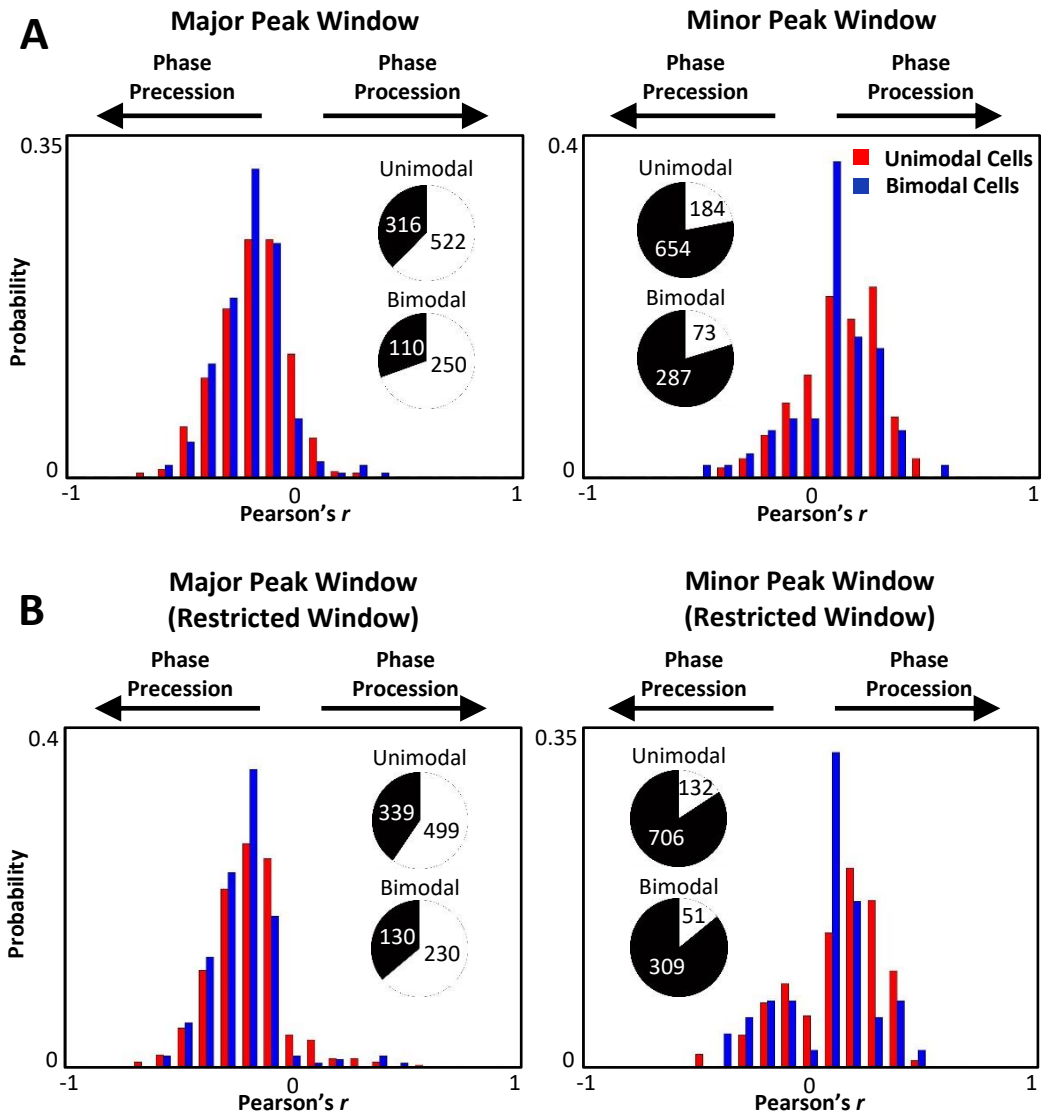

Fig. S15. Distributions of correlations between spike phase and normalized position. For each unimodal and bimodal cell across all open field and linear track sessions, if it fired more than 100 spikes within its place field during running periods (velocity ≥ 10 cm/s), the linear Pearson's correlation was quantified between the theta phase at which each spike occurred and the normalized position of the rat when the spike occurred. The correlations were restricted to spikes with phases in the major peak (left) or minor peak (right) windows. For linear track sessions, UP and DOWN runs were independently analyzed. **(A)** Distribution of Pearson's *r* values for all significant correlations in the major peak or minor peak window for unimodal (red) or bimodal (blue) cells. Total number of cells with significant (white) or non-significant (black) correlations shown in inset. **(B)** To reduce the possibility of 'bleed-through' from the previous cycle, which might trivially produce artifactual correlations, the same linear correlation was performed, but the major peak window correlation used only normalized positions -1 to 0.5 and the minor peak window correlation used only normalized positions -0.5 to 1. In addition, each window was made 20° smaller (major peak window = 210° to 420°/60°; minor peak window = 90° to 180°. As **A**, the distribution of correlation *r* values for all significant correlations. Significance determined by t-distribution; $\alpha = 0.05$.

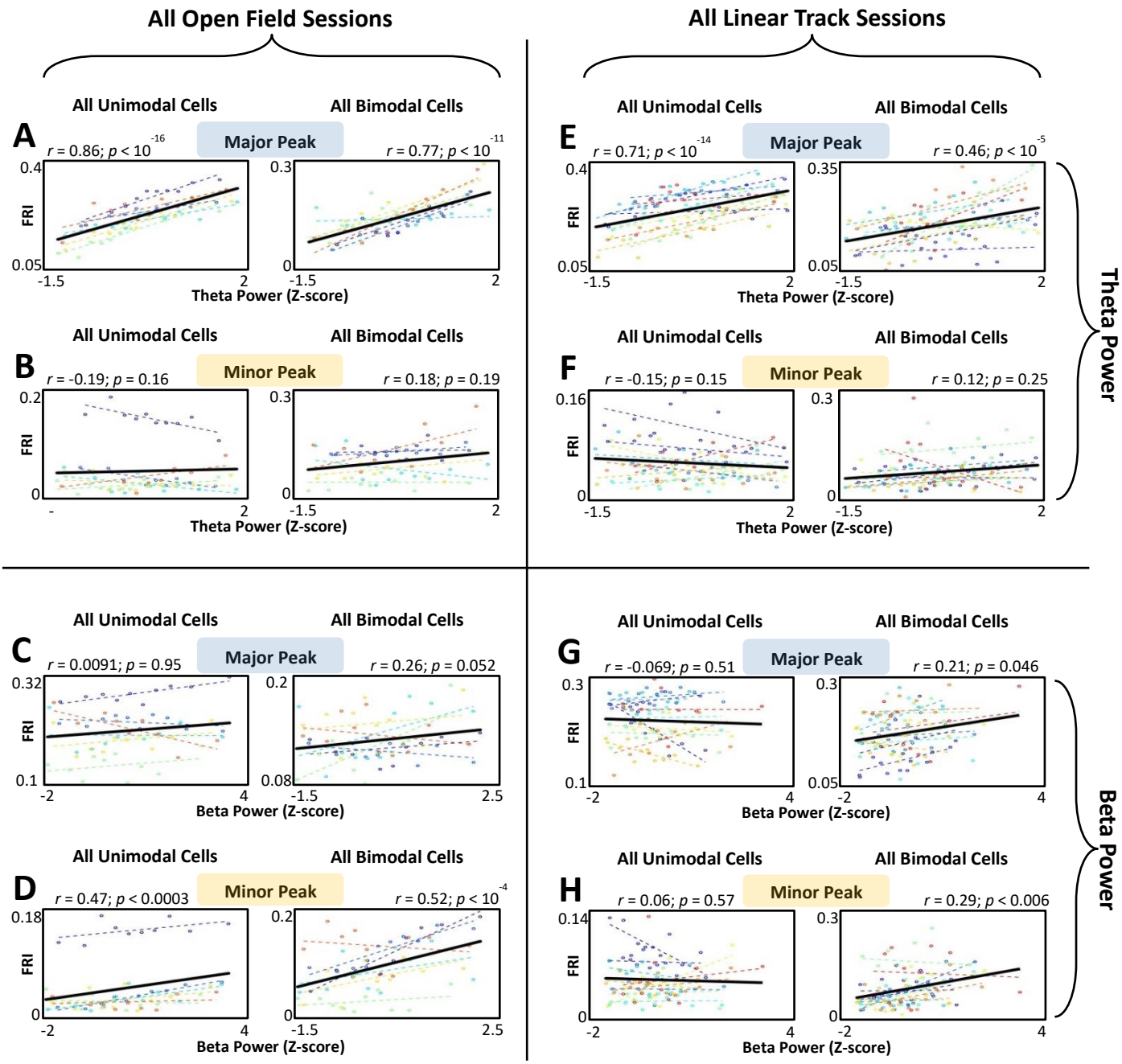

Fig. S16. Correlation between theta or beta power and neural activity in the major peak or minor peak windows for open field and linear track sessions. Data as in Figure 4, but separated by environment type: open field (**A-D**) vs. linear track (**E-H**). **A, B, E,** and **F** quantify the effect of theta (6-12 Hz) power on firing in the forward vs. reverse window. **C, D, G,** and **H** quantify the effect of beta (15-20 Hz) power on firing in the forward vs. reverse window. Statistics based on repeated measurements of correlation.

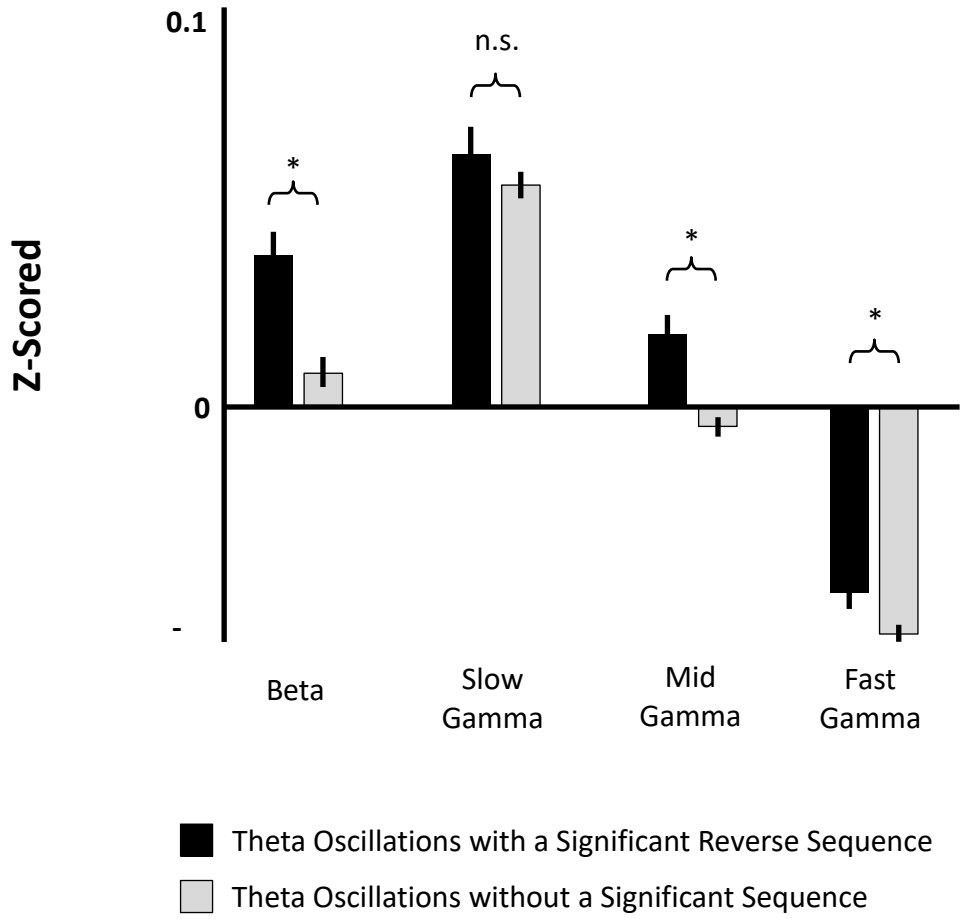

Fig. S17. Power of beta and gamma bands during significant forward and reverse sequences. For all open field and linear track sessions, the power of beta (15-20 Hz), slow gamma (30-50 Hz), mid gamma (65-90 Hz), and fast gamma (90-140 Hz) were each z-scored across the entire session. Plotted are the mean ± S.E.M. power of these z-scored frequency bands during theta oscillations that contained significant backward sequences in the reverse window vs. those that did not contain a significant sequence. * significant for corrected α (original $\alpha = 0.05$, Bonferroni-corrected $\alpha = 0.0125$); n.s. *p*-value > 0.2; Student's *t*-test with Bonferroni correction for four tests.

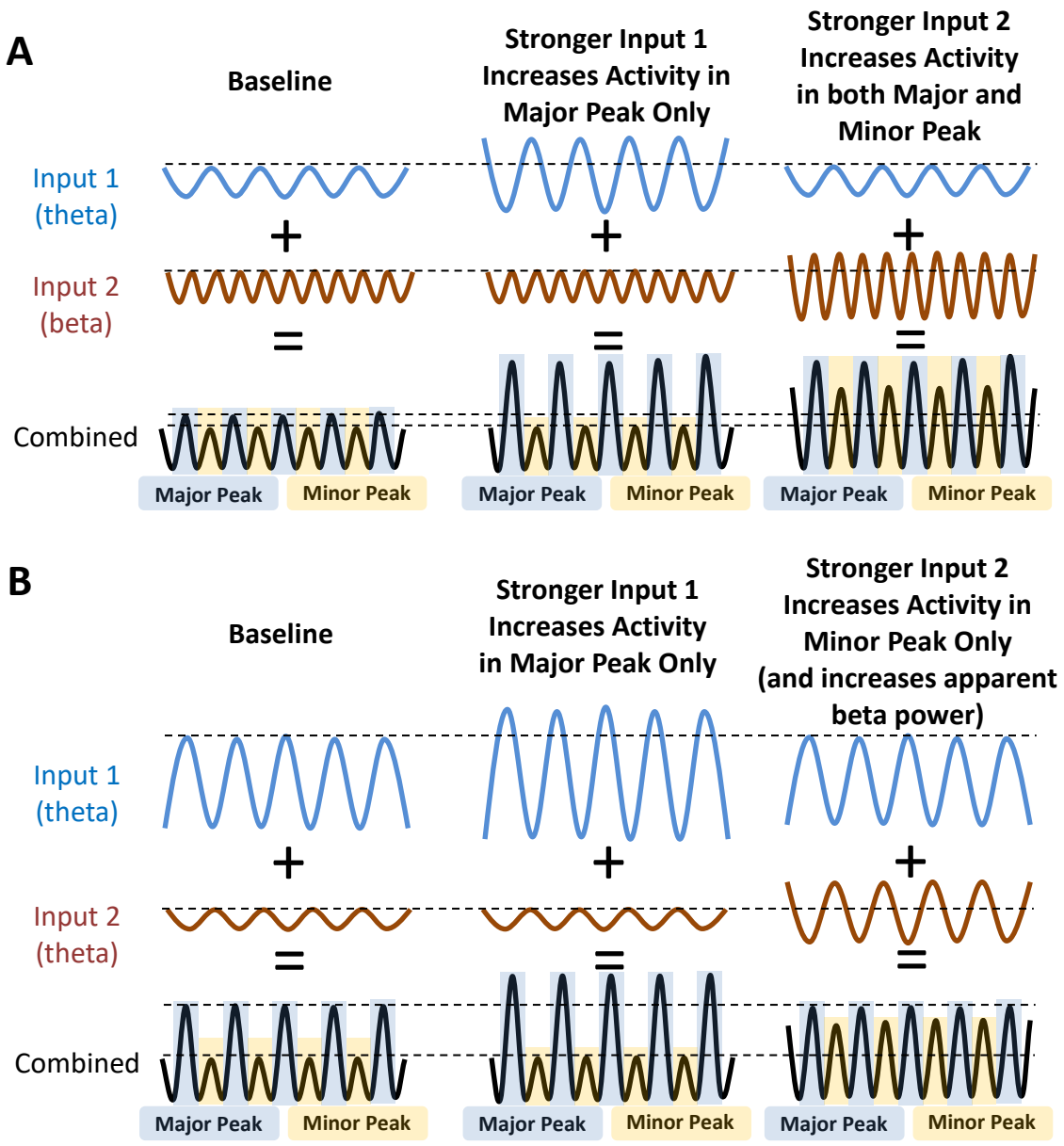

Fig. S18. Competing models of theta vs. beta frequency input. Two competing models describing how independent inputs may affect firing in the major peak (forward) and minor peak (reverse) windows. Horizontal dashed lines indicate baseline levels of Input 1, Input 2, and activity in major and minor peak windows. **(A)** This model assumes that CA1 receives a theta-frequency input and a beta-frequency input. The theta-frequency input drives firing in the major peak window, while the beta-frequency input drives firing in both major and minor peak windows. According to this model, if the beta-frequency input grows stronger, firing in both the major peak and minor peak should increase, which we do not observe (Fig 4). **(B)** This model assumes that CA1 receives two theta-frequency inputs that are roughly 180° phase-offset, which produces beta-frequency oscillatory activity in CA1. The first input drives firing at the major peak window and the second drives firing at the minor peak window. According to this model, increases in either of these inputs selectively affects firing in only one window, consistent with

our data (Fig 4). We presume that the theta-frequency input driving activity in the major peak window is considerably stronger than the input driving activity in the minor peak window. Thus, when we filter in the theta-frequency band, we selectively identify the stronger input, and changes in our observed theta-frequency power are reflective of changes in this input. We further presume that theta-frequency input driving activity in the minor peak window is weaker, but more dynamic (*i.e.*, it shows relatively larger changes in power). Thus, when we filter in the beta-band, we are identifying both theta-frequency inputs, but because the weaker input has a larger dynamic range, changes in beta power are more strongly reflective of the second input than the first.

Rat ID	Environment	Excitatory Cell Yield	Mean ± SEM Decoding Error (cm)	# of theta oscillations analyzed
1	Linear Track 1	124	9.38 ± 0.38	2,648
1	Linear Track 2	209	7.60 ± 0.19	6,537
1	Linear Track 3	200	6.90 ± 0.14	5,916
1	Linear Track 4	158	6.26 ± 0.23	2,340
1	Linear Track 5	145	6.71 ± 0.15	4,255
1	Linear Track 6	149	10.92 ± 0.44	2,921
1	Open Field 1	204	9.97 ± 0.24	9,633
1	Open Field 2	253	12.56 ± 0.23	16,454
2	Linear Track 1	133	8.91 ± 0.35	2,448
2	Linear Track 2	129	10.89 ± 0.20	4,661
2	Open Field 1	174	17.87 ± 0.41	10,855
2	Open Field 2	153	27.91 ± 0.55	11,587
3	Linear Track 1	62	17.35 ± 0.52	5,460
3	Linear Track 2	58	14.21 ± 0.50	4,223
3	Open Field 1	79	22.05 ± 0.46	12,998
3	Open Field 2	79	22.71 ± 0.47	12,909

Table S1. Experimental conditions. For each experiment, the rat ID, behavioral environment in which the data was recorded, the total excitatory cell yield, the mean ± SEM decoding error (Euclidean distance from rat's actual location to the location of peak posterior probability in each Bayesian decoding window using non-overlapping 250 ms windows) in cm, and the total number of theta oscillations analyzed.

References and Notes

1. D. J. Foster, M. A. Wilson, Reverse replay of behavioural sequences in hippocampal place cells during the awake state. *Nature* **440**, 680–683 (2006). doi:10.1038/nature04587 Medline

2. K. Diba, G. Buzsáki, Forward and reverse hippocampal place-cell sequences during ripples. *Nat. Neurosci.* **10**, 1241–1242 (2007). doi:10.1038/nn1961 Medline

3. G. E. Wimmer, Y. Liu, N. Vehar, T. E. J. Behrens, R. J. Dolan, Episodic memory retrieval success is associated with rapid replay of episode content. *Nat. Neurosci.* **23**, 1025–1033 (2020). doi:10.1038/s41593-020-0649-z Medline

4. D. Robbe, G. Buzsáki, Alteration of theta timescale dynamics of hippocampal place cells by a cannabinoid is associated with memory impairment. *J. Neurosci.* **29**, 12597–12605 (2009). doi:10.1523/JNEUROSCI.2407-09.2009 Medline

5. K. A. Bolding, J. Ferbinteanu, S. E. Fox, R. U. Muller, Place cell firing cannot support navigation without intact septal circuits. *Hippocampus* **30**, 175–191 (2020). doi:10.1002/hipo.23136 Medline

6. W. E. Skaggs, B. L. McNaughton, M. A. Wilson, C. A. Barnes, Theta phase precession in hippocampal neuronal populations and the compression of temporal sequences. *Hippocampus* **6**, 149–172 (1996). doi:10.1002/(SICI)1098-1063(1996)6:2<149:AID-HIPO6>3.0.CO;2-K Medline

7. G. Dragoi, G. Buzsáki, Temporal encoding of place sequences by hippocampal cell assemblies. *Neuron* **50**, 145–157 (2006). doi:10.1016/j.neuron.2006.02.023 Medline

8. A. S. Gupta, M. A. van der Meer, D. S. Touretzky, A. D. Redish, Segmentation of spatial experience by hippocampal θ sequences. *Nat. Neurosci.* **15**, 1032–1039 (2012). doi:10.1038/nn.3138 Medline

9. K. Kay, J. E. Chung, M. Sosa, J. S. Schor, M. P. Karlsson, M. C. Larkin, D. F. Liu, L. M. Frank, Constant Sub-second Cycling between Representations of Possible Futures in the Hippocampus. *Cell* **180**, 552–567.e25 (2020). doi:10.1016/j.cell.2020.01.014 Medline

10. C. Drieu, R. Todorova, M. Zugaro, Nested sequences of hippocampal assemblies during behavior support subsequent sleep replay. *Science* **362**, 675–679 (2018). doi:10.1126/science.aat2952 Medline

11. B. E. Pfeiffer, D. J. Foster, Hippocampal place-cell sequences depict future paths to remembered goals. *Nature* **497**, 74–79 (2013). doi:10.1038/nature12112 Medline

12. B. E. Pfeiffer, D. J. Foster, Autoassociative dynamics in the generation of sequences of hippocampal place cells. *Science* **349**, 180–183 (2015). doi:10.1126/science.aaa9633 Medline

13. B. L. McNaughton, C. A. Barnes, J. O'Keefe, The contributions of position, direction, and velocity to single unit activity in the hippocampus of freely-moving rats. *Exp. Brain Res.* **52**, 41–49 (1983). doi:10.1007/BF00237147 Medline

14. A. Fernández-Ruiz, A. Oliva, G. A. Nagy, A. P. Maurer, A. Berényi, G. Buzsáki, Entorhinal-CA3 Dual-Input Control of Spike Timing in the Hippocampus by Theta-Gamma Coupling. *Neuron* **93**, 1213–1226.e5 (2017). doi:10.1016/j.neuron.2017.02.017 Medline

15. K. Mizuseki, K. Diba, E. Pastalkova, G. Buzsáki, Hippocampal CA1 pyramidal cells form functionally distinct sublayers. *Nat. Neurosci.* **14**, 1174–1181 (2011). doi:10.1038/nn.2894 Medline

16. N. B. Danielson, J. D. Zaremba, P. Kaifosh, J. Bowler, M. Ladow, A. Losonczy, Sublayer-Specific Coding Dynamics during Spatial Navigation and Learning in Hippocampal Area CA1. *Neuron* **91**, 652–665 (2016). doi:10.1016/j.neuron.2016.06.020 Medline

17. J. O'Keefe, M. L. Recce, Phase relationship between hippocampal place units and the EEG theta rhythm. *Hippocampus* **3**, 317–330 (1993). doi:10.1002/hipo.450030307 Medline

18. Y. Yamaguchi, Y. Aota, B. L. McNaughton, P. Lipa, Bimodality of theta phase precession in hippocampal place cells in freely running rats. *J. Neurophysiol.* **87**, 2629–2642 (2002). doi:10.1152/jn.2002.87.6.2629 Medline

19. C. S. Lansink, G. T. Meijer, J. V. Lankelma, M. A. Vinck, J. C. Jackson, C. M. A. Pennartz, Reward Expectancy Strengthens CA1 Theta and Beta Band Synchronization and Hippocampal-Ventral Striatal Coupling. *J. Neurosci.* **36**, 10598–10610 (2016). doi:10.1523/JNEUROSCI.0682-16.2016 Medline

20. J. D. Berke, V. Hetrick, J. Breck, R. W. Greene, Transient 23-30 Hz oscillations in mouse hippocampus during exploration of novel environments. *Hippocampus* **18**, 519–529 (2008). doi:10.1002/hipo.20435 Medline

21. L. M. Rangel, A. A. Chiba, L. K. Quinn, Theta and beta oscillatory dynamics in the dentate gyrus reveal a shift in network processing state during cue encounters. *Front. Syst. Neurosci.* **9**, 96 (2015). doi:10.3389/fnsys.2015.00096 Medline

22. E. W. Schomburg, A. Fernández-Ruiz, K. Mizuseki, A. Berényi, C. A. Anastassiou, C. Koch, G. Buzsáki, Theta phase segregation of input-specific gamma patterns in entorhinal-hippocampal networks. *Neuron* **84**, 470–485 (2014). doi:10.1016/j.neuron.2014.08.051 Medline

23. M. Valero, L. M. de la Prida, The hippocampus in depth: A sublayer-specific perspective of entorhinal-hippocampal function. *Curr. Opin. Neurobiol.* **52**, 107–114 (2018). doi:10.1016/j.conb.2018.04.013 Medline

24. A. Navas-Olive, M. Valero, T. Jurado-Parras, A. de Salas-Quiroga, R. G. Averkin, G. Gambino, E. Cid, L. M. de la Prida, Multimodal determinants of phase-locked dynamics across deep-superficial hippocampal sublayers during theta oscillations. *Nat. Commun.* **11**, 2217 (2020). doi:10.1038/s41467-020-15840-6 Medline

25. L. L. Colgin, T. Denninger, M. Fyhn, T. Hafting, T. Bonnevie, O. Jensen, M.-B. Moser, E. I. Moser, Frequency of gamma oscillations routes flow of information in the hippocampus. *Nature* **462**, 353–357 (2009). doi:10.1038/nature08573 Medline

26. R. A. Koene, M. E. Hasselmo, Reversed and forward buffering of behavioral spike sequences enables retrospective and prospective retrieval in hippocampal regions CA3 and CA1. *Neural Netw.* **21**, 276–288 (2008). doi:10.1016/j.neunet.2007.12.029 Medline

27. T. Haga, T. Fukai, Recurrent network model for learning goal-directed sequences through reverse replay. *eLife* **7**, e34171 (2018). doi:10.7554/eLife.34171 Medline

28. E. Arrigoni, R. W. Greene, Schaffer collateral and perforant path inputs activate different subtypes of NMDA receptors on the same CA1 pyramidal cell. *Br. J. Pharmacol.* **142**, 317–322 (2004). doi:10.1038/sj.bjp.0705744 Medline

29. A. Aksoy-Aksel, D. Manahan-Vaughan, The temporoammonic input to the hippocampal CA1 region displays distinctly different synaptic plasticity compared to the Schaffer collateral input in vivo: Significance for synaptic information processing. *Front. Synaptic Neurosci.* **5**, 5 (2013). doi:10.3389/fnsyn.2013.00005 Medline

30. H. Takahashi, J. C. Magee, Pathway interactions and synaptic plasticity in the dendritic tuft regions of CA1 pyramidal neurons. *Neuron* **62**, 102–111 (2009). doi:10.1016/j.neuron.2009.03.007 Medline

31. J. Basu, J. D. Zaremba, S. K. Cheung, F. L. Hitti, B. V. Zemelman, A. Losonczy, S. A. Siegelbaum, Gating of hippocampal activity, plasticity, and memory by entorhinal cortex long-range inhibition. *Science* **351**, aaa5694 (2016). doi:10.1126/science.aaa5694 Medline

32. A. M. Wikenheiser, A. D. Redish, The balance of forward and backward hippocampal sequences shifts across behavioral states. *Hippocampus* **23**, 22–29 (2013). doi:10.1002/hipo.22049 Medline

33. K. W. Bieri, K. N. Bobbitt, L. L. Colgin, Slow and fast γ rhythms coordinate different spatial coding modes in hippocampal place cells. *Neuron* **82**, 670–681 (2014). doi:10.1016/j.neuron.2014.03.013 Medline

34. A. Cei, G. Girardeau, C. Drieu, K. E. Kanbi, M. Zugaro, Reversed theta sequences of hippocampal cell assemblies during backward travel. *Nat. Neurosci.* **17**, 719–724 (2014). doi:10.1038/nn.3698 Medline

35. M. Wang, D. Foster, B. Pfeiffer, Data from "Alternating sequences of future and past behavior encoded within hippocampal theta oscillations," Zenodo (2020); doi:10.5281/zenodo.3972156.

36. T. J. Davidson, F. Kloosterman, M. A. Wilson, Hippocampal replay of extended experience. *Neuron* **63**, 497–507 (2009). doi:10.1016/j.neuron.2009.07.027 Medline

37. J. Z. Bakdash, L. R. Marusich, Repeated Measures Correlation. *Front. Psychol.* **8**, 456 (2017). doi:10.3389/fpsyg.2017.00456 Medline

38. R. E. Ambrose, B. E. Pfeiffer, D. J. Foster, Reverse Replay of Hippocampal Place Cells Is Uniquely Modulated by Changing Reward. *Neuron* **91**, 1124–1136 (2016). doi:10.1016/j.neuron.2016.07.047 Medline